CONDENSED MATTER PHYSICS

# Real-space observation of fluctuating antiferromagnetic domains

**Min Gyu Kim[1,2], Andi Barbour[3], Wen Hu[3], Stuart B. Wilkins[3], Ian K. Robinson[4], Mark P. M. Dean[4], Junjie Yang[5], Choongjae Won[6,7], Sang-Wook Cheong[1,6,7,8], Claudio Mazzoli[3], Valery Kiryukhin[1]***



**Magnetic domains play a fundamental role in physics of magnetism and its technological applications. Dynamics of antiferromagnetic domains is poorly understood, although antiferromagnets are expected to be extensively used in future electronic devices wherein it determines the stability and operational speed. Dynamics of antiferromagnets also features prominently in the studies of topological quantum matter. Real-space imaging of fluctuating antiferromagnetic domains is therefore highly desired but has never been demonstrated. We use coherent x-ray diffraction to obtain videos of fluctuating micrometer-scale antiferromagnetic domains in $Ni_2MnTeO_6$ on time scales from $10^{-1}$ to $10^3$ s. In the collinear phase, thermally activated domain wall motion is observed in the vicinity of the Néel temperature. Unexpectedly, the fluctuations persist through the full range of the higher-temperature helical phase. These observations illustrate the high potential significance of the dynamic domain imaging in phase transition studies and in magnetic device research.**

## INTRODUCTION

Dynamics of magnetic domains has been a subject of intense studies ever since the observation of magnetoacoustic domain switching noise by Barkhousen more than a century ago (*1*). Performance of magnetic storage media is defined by the achievable domain switching rates and by the thermal stability of the domains. Domain switching and fluctuations involve the formation and motion of the domain walls. In addition to the obvious technological importance, domain wall dynamics is of the fundamental relevance to the physics of phase transitions in a variety of subjects, ranging from condensed matter physics to the cosmology of the early universe (*2*). Historically, antiferromagnetic (AFM) domains attracted little attention, both because of the prevalence of ferromagnetism in technology and because of the difficulty of their observation. Recently, the situation changed markedly, largely because of two interconnected developments. First, it was realized that antiferromagnets may have several key advantages in prospective electronic devices (*3*, *4*). They exhibit vastly faster switching rates than ferromagnets and are better suited for miniaturization because of the reduced stray fields. Novel device concepts were proposed, giving rise to the field called AFM spintronics (*3*, *4*). Magnetic racetrack memory based on the current-driven motion of domain walls in a synthetic antiferromagnet is currently at the advanced engineering stage (*5*). AFM-based nonvolatile programmable synapses for artificial neural networks (*6*) and multilevel bit cells (*7*) are also being developed (*8*). Some of the existing memory cells already use AFM elements (*9*). In all these cases, the reliability and the operation speed are determined by the microscopic domain structure and the dynamics of the domain walls. Second, recent revolutionary developments in the field of topological quantum matter (*10*–*12*) brought about a plethora of exotic properties in antiferromagnets, many of them protected against external perturbations. They include the AFM anomalous (*13*, *14*) and topological (*15*, *16*) Hall effects, as well as the anomalous Nernst effect (*17*). It was quickly realized that these properties open new opportunities for spintronic devices (*18*, *19*), bringing in the field of topological AFM spintronics (*19*). Examples include a topological AFM transistor using Dirac quasiparticle current (*19*), a Majorana qubit in a quantum spin Hall insulator combined with AFM superconductor (*20*), and a skyrmion racetrack memory (*21*). There is an amazing interplay between the practical issues of spintronics and the advanced fundamental subjects of solid-state physics.

Imaging the AFM domain texture and the dynamics of the domain walls is essential for engineering spintronics devices, as well as for measurements of the intrinsic topological properties in quantum matter. AFM domain dynamics is accessible to some existing spectroscopic techniques, such as x-ray photon correlation spectroscopy (XPCS) (*22*, *23*). However, unlike imaging, they measure the characteristic time scales, not the real-space positions of the domain walls. Imaging AFM domains is a notoriously difficult task even for static structures (*24*). Dynamic imaging is currently impossible for practically all existing techniques including, particularly, scanning-based approaches. Perhaps the only method suitable for time-resolved studies is x-ray photoemission electron microscopy (PEEM) (*24*, *25*). In this technique, the AFM domain contrast is based on linear dichroism. Therefore, PEEM is only applicable to the domains distinguished by distinct spin direction axes. These domains often exhibit magnetostriction-induced macroscopic strain that may hinder their growth and fluctuations. This could be an important reason why no thermal fluctuations of AFM domains have so far been observed using x-ray PEEM. In contrast, AFM phase domains only involve changes of the order parameter phase across the domain wall. At the antiphase domain wall, for example, all the spins simply reverse their directions. Phase domains could be more susceptible to thermal fluctuations because they are not associated with macroscopic structural distortions. Recently, a new domain wall imaging technique based on destructive interference of

[1]Department of Physics and Astronomy, Rutgers University, Piscataway, NJ 08854, USA. [2]Department of Physics, University of Wisconsin-Milwaukee, Milwaukee, WI 53201, USA. [3]National Synchrotron Light Source II, Brookhaven National Laboratory, Upton, NY 11973, USA. [4]Condensed Matter Physics and Materials Science Department, Brookhaven National Laboratory, Upton, NY 11973, USA. [5]Department of Physics, New Jersey Institute of Technology, Newark, NJ 07102, USA. [6]Max Planck POSTECH/Korea Research Initiative, Pohang University of Science and Technology, Pohang 37673, Korea. [7]Laboratory of Pohang Emergent Materials, Department of Physics, Pohang University of Science and Technology, Pohang 37673, Korea. [8]Rutgers Center for Emergent Materials, Rutgers University, Piscataway, NJ 08854, USA.
*Corresponding author. Email: vkir@physics.rutgers.edu

coherent x-rays in a diffraction experiment has been reported (*26*). It is applicable to phase domains and takes an image in a single-exposure measurement. Here, we use an enhanced version of this approach to study the real-space thermal evolution of the AFM domains in $Ni_2MnTeO_6$ and obtain real-time videos of the fluctuating domain walls.

## RESULTS

$Ni_2MnTeO_6$ is a rhombohedral (space group *R*3) $A_2BB'O_6$-type corundum derivative (*27*). For $T < T_{N1} = 68.0$ K, it is a *c* axis collinear antiferromagnet with the magnetic structure shown in Fig. 1A. At higher temperatures, $Ni_2MnTeO_6$ exhibits an incommensurate helical (proper screw) state (see Fig. 1B) (*28*). The spins rotate in the *ab* plane, and the propagating vector is along the *c* axis with the period very close to three structural lattice units. The sample is paramagnetic above $T_{N2} = 74.0$ K. The collinear and the helical states give rise to magnetic x-ray diffraction peaks at $Q_C = (0, 0, 1.5)$ and $Q_{IC} = (0, 0, 1.354)$, respectively. Their intensities versus temperature are shown in Fig. 1C. There is a phase coexistence region between 66 and 68 K, indicating that the transition is first order. No hysteresis is observed. The collinear state should exhibit simple antiphase domains. Assuming an exact tripling of the unit cell in the helical state, up to six different domain types are possible because the order parameter phase at the domain wall can change by $\pi$ and $\pm 2\pi/3$. Complex domain textures, including topological $Z_n$ vortices similar to those observed in ferroelectrics (*29*, *30*), are therefore possible in the helical state.

We use the method (*26*) in which the magnetic texture image is formed by the coherent x-ray beam reflected from the *ab* surface of the sample (see Fig. 1D). Imaging is done under the magnetic Bragg diffraction condition, which results in purely magnetic scattering.

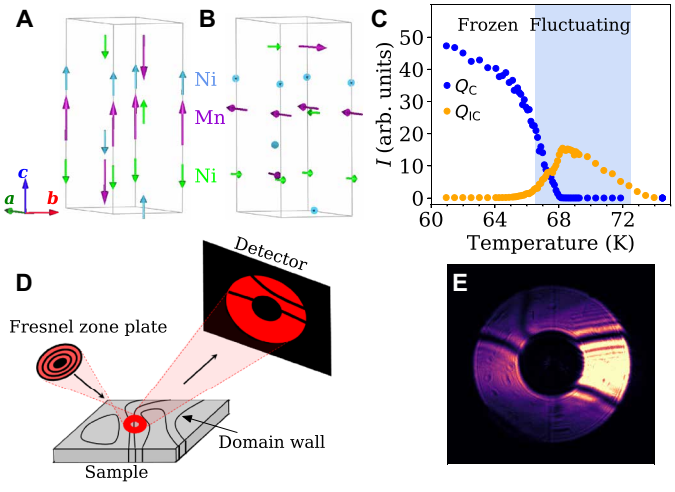


**Fig. 1. Magnetic structures and experimental setup.** Magnetic structure of the collinear (**A**) and the helical (**B**) states of $Ni_2MnTeO_6$. One structural unit cell is shown for simplicity. On moving from one such cell to the next along the *c* axis, the spins rotate by 180° in (A) and by ~120° in the *ab* plane in (B). (**C**) The temperature dependence of the intensities of the $Q_C = (0, 0, 1.5)$ and $Q_{IC} = (0, 0, 1.354)$ magnetic Bragg peaks produced by the collinear and the helical states, respectively. The shaded area indicates the region where the AFM domain fluctuations are observed. (**D**) Schematic setup of the imaging experiment. The domain walls are imaged as dark lines on the area detector (**E**).

Signal intensity is maximized by setting the x-ray energy at Ni $L_{III}$ edge. Fully separate contributions can be accessed from the collinear state at a scattering vector $Q = Q_C$ and from the helical state for $Q = Q_{IC}$. The AFM domain walls are imaged as dark lines on the area detector because of the destructive interference between the parts of the beam scattered from the adjacent AFM phase domains. Undistorted (except for the trivial beam footprint correction) real-space images of the domain walls in the specific magnetic state are obtained in a single-exposure measurement. Previously, the incident x-ray beam was formed by a pinhole (*26*). In that approach, the image is formed far in the wings of the scattered beam, making the majority of the available photons useless for the imaging. Diffraction effects limit the achievable spatial resolution (the minimum size of the resolvable domains) to approximately the pinhole size *d*. This resolution is only achieved for a pinhole-sample distance of order of $d^2/\lambda$, where $\lambda$ is the x-ray wavelength. This condition gives impractically small distances for resolutions approaching 1 μm. To overcome these drawbacks, we used a Fresnel zone plate (FZP) to form the incident beam. The entire annular-shaped beam produced by the FZP can be used in imaging (see Fig. 1E), providing for better utilization of the available photons and decreased exposure times. FZP is a focusing device. The beam divergence and the image magnification can therefore be controlled by the FZP design. The effective source can be easily put at small distances to the sample, as required to obtain the increased spatial resolution. This should eventually make the ultimate spatial resolution of the method possible. In bulk samples, it is roughly set by the x-ray penetration depth, which lies in the 100- to 200-nm range in typical *3d*-element magnets at their respective *L* edge x-ray energies. Better resolutions might be possible in thin films, as discussed in the Supplementary Materials. The high intensity and the controlled effective source position of the divergent x-ray beam produced by the FZP were crucial improvements resulting in the temporal and spatial resolutions necessary to observe AFM domain wall fluctuations.

We first discuss the collinear state, starting with the big-picture temperature-dependent evolution of the AFM domain pattern. The coarse resolution of the pinhole setup was sufficient for this task. Figure 2 shows that very small domains appear just below $T_{N1}$. They merge and grow with decreasing temperature. Different textures are observed. In the lower right corner, a fine stripy pattern is first formed. It evolves into large domains preserving the stripe motif. Less-regular domain shapes are observed near the image center. Entropy-driven proliferation of domain walls is expected on approaching the phase transition temperature, as the domain wall formation energy is reduced with decreasing order parameter. Our experiments demonstrate this general scenario in an antiferromagnet.

Thermal fluctuations of the AFM domain walls become evident when the spatial resolution is improved beyond 4 μm, with image capture times in the $10^{-2}$ s range. Detailed discussion of the obtained resolutions can be found in the Supplementary Materials. Movies of the fluctuating domains with the capture time of $5.75 \times 10^{-2}$ s and the full frame length of 0.195 s were recorded, some of them as long as ~20 min. Movie S1 shows the data collected at $T = 67.73$ K; the examples discussed below are taken from this movie. A rich variety of the dynamic behavior types was observed, including a continuous domain wall deformation, a fast back and forth switching between two states, and more complex scenarios. Figure 3A depicts selected frames, showing a continuously growing bulge in a domain wall. (See movie S2 for the corresponding full movie.) To

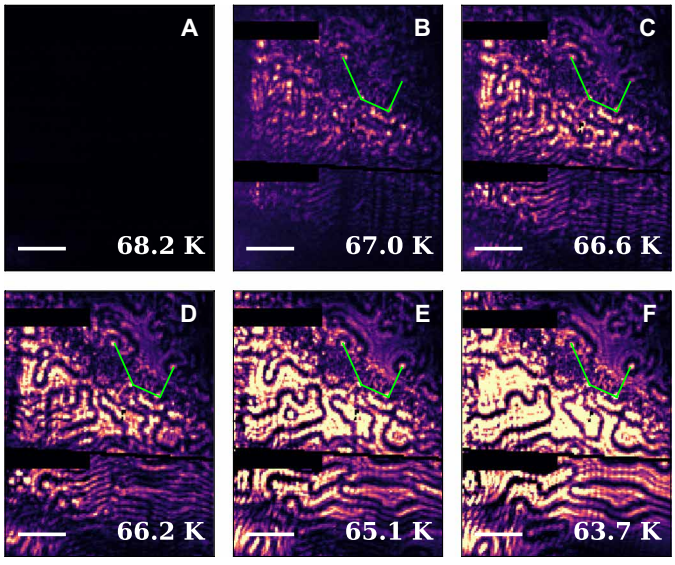


**Fig. 2. Thermal evolution of the AFM domains.** (**A** to **F**) Images of the AFM domain boundaries (dark wavy lines) in the collinear state, taken on cooling through the transition temperature $T_{N1}$. Straight green lines connect four structural defects occurring in the same positions in all images, providing the positional reference. Black rectangles are detector dead zones. Scale bars, 10 μm. They show distances on the sample surface.

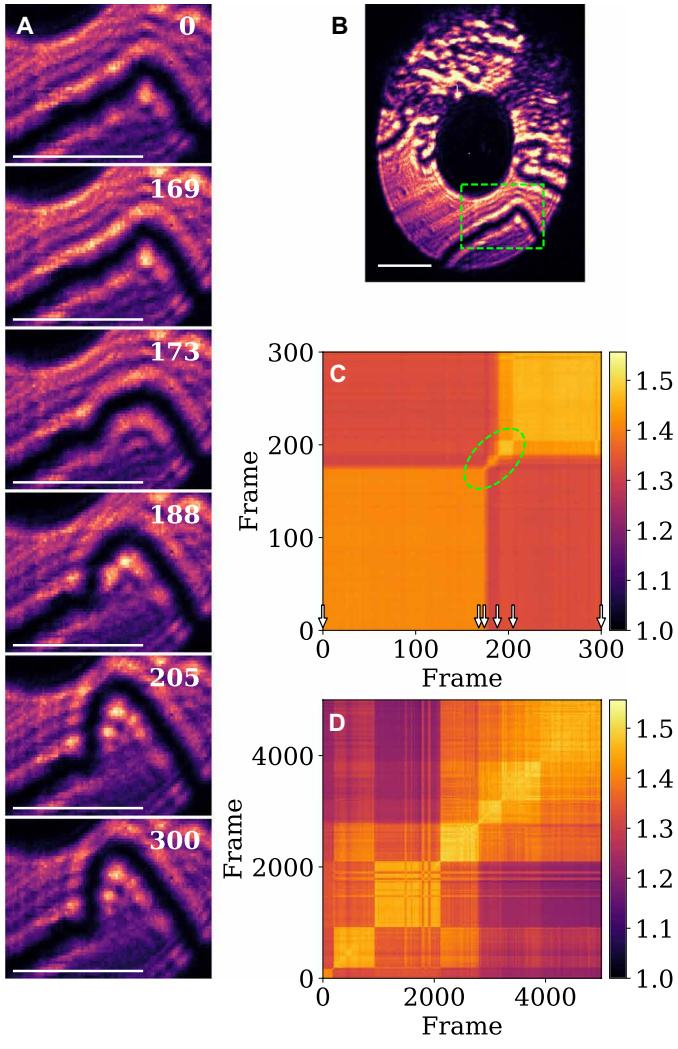


**Fig. 3. Bulge growth in the domain wall.** (**A**) Selected frames showing time-dependent evolution of a bulging domain wall in the collinear state at $T = 67.73$ K. The frames are taken from the detector area outlined with the green box in (**B**). (**C** and **D**) The two-time correlation function $G(t_1, t_2)$ for the same area for different time intervals. The green oval in (C) indicates the region in which the changes occur. The images are static outside this region. Frame numbers are listed for each panel in (A). The same frames are indicated with white arrows in (C). The frame capture time is $5.75 \times 10^{-2}$ s, and the time between consecutive frames is 0.195 s. Scale bars, 10 μm (A and B).

extract the characteristic time scales from the dynamic images, we use the two-time correlation function $G(t_1, t_2) = \langle I(t_1)I(t_2)\rangle / \langle I(t_1)\rangle\langle I(t_2)\rangle$, which is a common tool in XPCS (*31*). $I(t)$ is the intensity, and the averaging is taken over the images on a pixel-by-pixel basis. Figure 3C shows $G(t_1, t_2)$ for the time interval relevant to Fig. 3A. Bright uniform squares with diagonals along the $t_1 = t_2$ line correspond to highly correlated and, therefore, essentially static images. Figure 3C provides a clear visual evidence (large orange square in the lower left corner), showing that the domain wall is mostly static from frame 0 to 169. Then, a series of changes on the time scales ranging from a single to several frames over the period of 36 frames (6.8 s) takes place, and then the image stays static again. Figure 3D depicts $G(t_1, t_2)$ for an extended period of time (16 min). It shows that the deformations of this bulging and moving domain wall occur in the broad range of time scales, from ≤0.2 s (one frame) to minutes.

Figure 4A illustrates a different fluctuation type—fast back and forth jumps of the domain wall between the two positions shown by vertical blue arrows—the so-called two-state switching. The jumps occur over one frame (faster than 0.2 s), producing the narrow dark lines in $G(t_1, t_2)$ shown in Fig. 4B. The extended-time $G(t_1, t_2)$ depicted in Fig. 4C illustrates that the fast back and forth switching events keep occurring in the area of interest, separated by the intervals from 0.2 s (smallest resolvable) to many seconds. This range overlaps with the field-induced domain switching time scales observed in the famous Barkhousen effect in ferromagnets. The surface regions shown in Figs. 3 and 4 exhibit two different types of dynamic behavior, continuous motion and two-state switching. In XPCS experiments, $G(t_1, t_2)$ patterns similar to ours are taken as evidence for such behavior based on plausible models (*32*). Our real-space measurements provide model-independent examples illustrating the validity of this approach. Other thermal fluctuation types can be observed in the full movie, such as formation and disappearance of bubble domains (horizontal green arrows in Fig. 4A). The observed fluctuations characterize the steady state of the system because they persist over the time of the experiment (hours). Because of the local beam heating, thermal gradients and the corresponding heat currents might exist on the sample surface, possibly affecting the dynamics of the domain walls. While localized directional domain wall motion such as shown in Fig. 3 is observed, we do not find any clear evidence of the preferred direction (e.g., motion toward or away from the image center) in the entire image area. This shows that the effects of the thermal gradients are probably small. Measurements under various local thermal conditions are needed to establish whether the inhomogeneities induce deviations

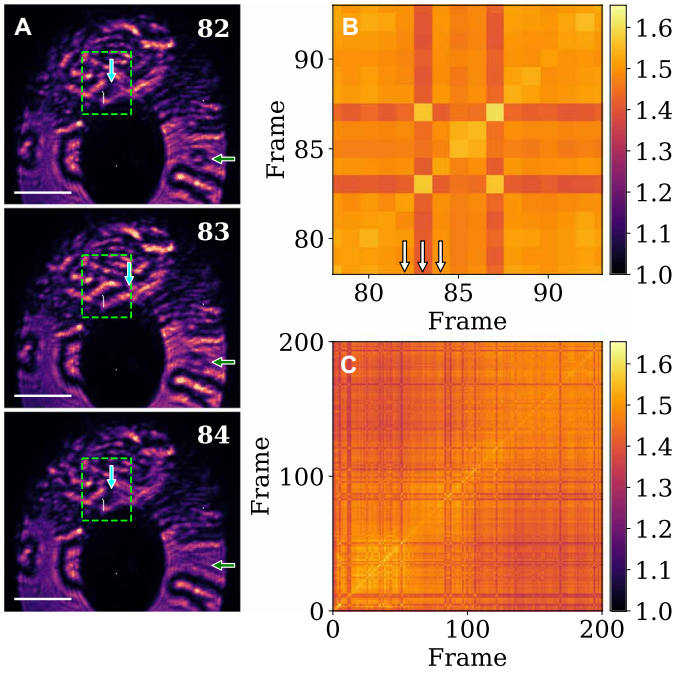


**Fig. 4. Two-state switching fluctuations.** (**A**) Consecutive frames showing back and forth domain wall jumps, denoted by vertical blue arrows, in the collinear state at $T = 67.73$ K. Disappearance of a bubble domain is also evident (green arrows). (**B** and **C**) $G(t_1, t_2)$ for the detector area outlined with the green box in (A) for compressed and expanded time intervals. Frame numbers are listed for each panel in (A). The same frames are indicated with white arrows in (B). The frame capture time is $5.75 \times 10^{-2}$ s, and the time between consecutive frames is 0.195 s. Scale bars, 10 μm (A).

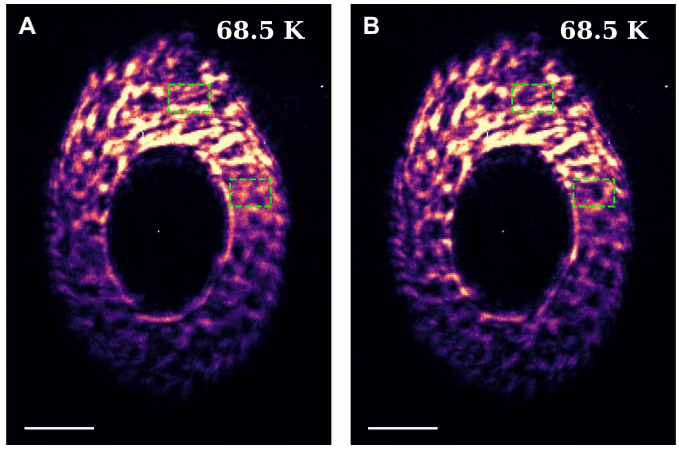


**Fig. 5. Fluctuations in the helical state.** (**A** and **B**) Two consecutive detector images at the helical state wave vector at $T = 68.5$ K. Green boxes outline the areas with noticeable changes. The image capture time is $5.75 \times 10^{-2}$ s, and the time between the images is 0.195 s. Scale bars, 10 μm.

from the equilibrium behavior in our experiments. This is the subject of future work. To take the full advantage of the great wealth of information contained in the movies of the fluctuating domains, development of image analysis tools applicable to combined spatial (domain wall positions) and temporal information is highly desired. On a qualitative level, the data of Figs. 3 and 4, as well as cursory observation of the full movies, indicate that the high-curvature regions of the domain walls are more susceptible to thermal motion. This behavior is expected for any object with effective surface tension (energy), such as AFM domain walls.

Unlike the collinear state, the helical phase does not exhibit clear domain walls. Ripple-like patterns are observed instead (see Fig. 5). Higher-resolution studies are necessary to establish whether they reflect underlying domain structure or are more complex interference patterns from unresolvable nanoscale domains. Thermal fluctuations can, however, be reliably detected. Unexpectedly, they are present in the entire temperature range of the helical phase. Figure 5 shows fast fluctuations at $T = 68.5$ K, deep in the well-developed helical phase region, very far from any transition temperature and the phase coexistence region. Movie S3 presents these fluctuations in full detail. This observation is important because the helical phase would be presumed to be static based on the results of the commonly used techniques that are not directly sensitive to fluctuations, such as diffraction or bulk susceptibility measurements. As illustrated in Fig. 1C, domain wall fluctuations are observed in a remarkably large range of reduced temperatures $(T_N - T)/T_N \sim 0.1$ (more than 6 K), covering the entire helical phase and extending by 2 K into the collinear phase. The spins in $Ni_2MnTeO_6$ are quite isotropic, as indicated by the easy axis to easy plane transition at $T_{N1}$. Pinning effects are greatly reduced for the thick domain walls that are typical of isotropic systems, as known well for ferromagnets (*33*). The competition between the collinear and the helical phases may also exert destabilizing effects, further promoting the robust domain wall fluctuations in $Ni_2MnTeO_6$.

## DISCUSSION

Real-space videos of fluctuating AFM domains provide full information on the domain dynamics within the resolution of the method. The available signal intensity makes possible reducing the exposure times into the millisecond range. Existing x-ray area detectors are capable of $10^{-5}$ s readout time. We expect that our approach will be applicable to real-space studies of dynamic magnetic and structural textures on time scales covering at least seven orders of magnitude ($10^{-3}$ to $10^{4}$ s), with ultimate space resolutions into hundreds of nanometers in the bulk samples and probably better than 100 nm in thin films. In $Ni_2MnTeO_6$, this will allow detailed studies of domain topology in the fluctuating helical phase. Investigation of the phase coexistence region, in which the helical state should produce dark regions in the images of the collinear state and vice versa, would also be intriguing. Studies of the same sample area for different scattering vectors will be possible using suitable fiducial marks on the sample (*34*). To fully explore the capabilities of our technique, it is highly desirable to develop appropriate image analysis tools, possibly based on machine learning and using advanced correlation function methods. We believe that this method will provide valuable information for the studies of phase transitions and will be highly useful for the investigation of device-like structures both in spintronics and in studies of topological quantum matter, for example, in Hall effect–type measurements. Our observation of persistent domain fluctuations in what appears to be a static magnetic phase illustrates a high potential of dynamic real-space imaging in device engineering, especially for understanding the limits of device thermal stability. The newly achieved ability to obtain real-space videos

showing fluctuating AFM domains should find many other applications in physics, materials science, and engineering.

## MATERIALS AND METHODS

### Experimental design

The experiment involved sample synthesis and x-ray imaging parts, as described below.

### Sample synthesis

$Ni_2MnTeO_6$ single crystals were synthesized by the chemical vapor transport method. Stoichiometric amounts of NiO (99.9%), $MnCO_3$ (99.99%), and $TeO_2$ (99.99%) were ground and sintered at 800°C for 24 hours, followed by furnace cooling to room temperature. The process was repeated twice with an intermediate grinding. The resultant powder was then sealed with the $TeCl_4$ agent in an evacuated quartz tube and kept in a two-zone tube furnace for 1 week with the hot and cold ends at 780° and 680°C, respectively. Afterward, the quartz tube containing the single crystals was slowly cooled to room temperature. The samples are thin platelets with a typical size of 1 mm. They exhibit natural mirror-like *ab* surfaces. The single crystal's stoichiometry was confirmed by comparison of its magnetic susceptibility and the magnetic transition temperatures to those of well-characterized polycrystalline samples. Possible deviations from the stoichiometric formula should not exceed 10% of the nominal Ni and Mn concentrations. These possible deviations do not affect the magnetic structure.

### X-ray imaging

The imaging technique used in this work is based on resonant magnetic x-ray diffraction measurements. They were carried out at the Coherent Soft X-ray Scattering (CSX) beamline, National Synchrotron Light Source II, Brookhaven National Laboratory. The coherent x-ray beam was polarized in the scattering plane. Two incident beam setups were used. In the first setup, the beam propagated through a 5-μm pinhole located 6.5 mm before the sample, producing an Airy diffraction pattern. This was used to obtain images of the sample area 200 to 300 μm in diameter, as described in detail in (*26*). In the second setup, the beam was focused by an FZP followed by an order-sorting aperture, ensuring that only the first diffraction order from the FZP reaches the sample. The zeroth-order transmission was blocked by a 60-μm central beam stop, resulting in an annular shape of the focused beam. The FZP diameter and its outer zone width were 150 μm and 80 nm, respectively, resulting in the 8.2-mm focal length at the Ni $L_{III}$ edge (853 eV). Additional details of this setup can be found in (*35*). The diameter of the beam at the sample position was set at several values in the 15 to 80 μm range by controlling the FZP to sample distance. This corresponds to an image magnification on the detector varying from ~400 to 80. The signal was recorded by an in-vacuum charge-coupled device (CCD) area detector (Berkeley Fast CCD; up to 100 Hz of frame rate, 960 pixels by 960 pixels, a pixel size of 30 μm by 30 μm, and no polarization discrimination), located 34 cm away from the sample. We report intensity in arbitrary units. The sample was mounted on a multicircle in-vacuum diffractometer on the cold finger of a helium flow cryostat. X-ray energy was scanned in the vicinity of the Ni $L_{III}$ edge to maximize the resonant magnetic scattering intensity. X-ray scattering was measured in a specular reflection geometry off the native *ab* surface of the sample; the scattering angle 2θ was 104° for $Q_C$ and 90° for $Q_{IC}$. In this geometry, the direct image of the sample surface observed on the detector is compressed in the scattering plane (along the detector's vertical direction) by a factor of sin(θ) because of the beam footprint size effect. The detector images shown in this paper are elongated vertically by the factor of 1/sin(θ) to compensate for this compression. The images therefore feature identical length scale bars for the vertical and horizontal directions (uniform magnification). The length scale in the images corresponds to the actual distance on the sample surface. It was determined by observing the image shift after a calibrated shift of the sample in the x-ray beam.

### Statistical analysis

All errors are from counting statistics. In Fig. 1C, error bars are smaller than the symbol size. The analysis of the spatial resolutions achieved in the images is given in the Supplementary Materials.

## SUPPLEMENTARY MATERIALS

Supplementary material for this article is available at https://science.org/doi/10.1126/sciadv.abj9493

## REFERENCES AND NOTES


1. H. Barkhausen, Zwei mit Hilfe der neuen Verstärker entdeckte Erscheinugen. *Physik Z.* **20**, 401–403 (1919).
2. T. Kibble, Phase-transition dynamics in the lab and the universe. *Phys. Today* **60**, 47–52 (2007).
3. V. Baltz, A. Manchon, M. Tsoi, T. Moriyama, T. Ono, Y. Tserkovnyak, Antiferromagnetic spintronics. *Rev. Mod. Phys.* **90**, 015005 (2018).
4. O. Gomonay, T. Jungwirth, J. Sinova, Concepts of antiferromagnetic spintronics. *Phys. Status Solidi* **11**, 1700022 (2017).
5. S. Parkin, S. H. Yang, Memory on the racetrack. *Nat. Nanotech.* **10**, 195–198 (2015).
6. W. A. Borders, H. Akima, S. Fukami, S. Moriya, S. Kurihara, Y. Horio, S. Sato, H. Ohno, Analogue spin–orbit torque device for artificial-neural-network-based associative memory operation. *Appl. Phys. Express* **10**, 013007 (2017).
7. P. Wadley, B. Howells, J. Železný, C. Andrews, V. Hills, R. P. Campion, V. Novák, K. Olejník, F. Maccherozzi, S. S. Dhesi, S. Y. Martin, T. Wagner, J. Wunderlich, F. Freimuth, Y. Mokrousov, J. Kuneš, J. S. Chauhan, M. J. Grzybowski, A. W. Rushforth, K. W. Edmonds, B. L. Gallagher, T. Jungwirth, Electrical switching of an antiferromagnet. *Science* **351**, 587–590 (2016).
8. T. Jungwirth, J. Sinova, A. Manchon, X. Marti, J. Wunderlich, C. Felser, The multiple directions of antiferromagnetic spintronics. *Nat. Phys.* **14**, 200–203 (2018).
9. K. Akmaldinov, L. Frangoul, C. Ducruet, C. Portemont, J. Pereira, I. Joumard, B. Dienyl, J. Alvarez-Herault, V. Baltz, Correlation between disordered magnetic phases in ferromagnetic/antiferromagnetic thin films and device-to-device variability of exchange bias in spintronic applications. *IEEE Magn. Lett.* **6**, 3000404 (2015).
10. M. Z. Hasan, C. L. Kane, Colloquium: Topological insulators. *Rev. Mod. Phys.* **82**, 3045–3067 (2010).
11. X.-L. Qi, S.-C. Zhang, Topological insulators and superconductors. *Rev. Mod. Phys.* **83**, 1057–1110 (2011).
12. C.-K. Chiu, J. C. Y. Teo, A. P. Schnyder, S. Ryu, Classification of topological quantum matter with symmetries. *Rev. Mod. Phys.* **88**, 035005 (2016).
13. H. Chen, Q. Niu, A. H. MacDonald, Anomalous Hall effect arising from noncollinear antiferromagnetism. *Phys. Rev. Lett.* **112**, 017205 (2014).
14. S. Nakatsui, N. Kiyohara, T. Higo, Large anomalous Hall effect in a non-collinear antiferromagnet at room temperature. *Nature* **527**, 212–215 (2015).
15. B. Binz, A. Vishwanath, V. Aji, Theory of the helical spin crystal: A candidate for the partially ordered state of MnSi. *Phys. Rev. Lett.* **96**, 207202 (2006).
16. A. Neubauer, C. Pfleiderer, B. Binz, A. Rosch, R. Ritz, P. G. Niklowitz, P. Böni, Topological Hall effect in the A phase of MnSi. *Phys. Rev. Lett.* **102**, 186602 (2009).
17. M. Ikhlas, T. Tomita, T. Koretsune, M.-T. Suzuki, D. Nishio-Hamane, R. Arita, Y. Otani, S. Nakatsuji, Large anomalous Nernst effect at room temperature in a chiral antiferromagnet. *Nat. Phys.* **13**, 1085–1090 (2017).
18. M. B. Jungfleisch, W. Zhang, A. Hoffmann, Perspectives of antiferromagnetic spintronics. *Phys. Lett. A* **382**, 865–871 (2018).
19. L. Šmejkal, Y. Mokrousov, B. Yan, A. H. MacDonald, Topological antiferromagnetic spintronics. *Nat. Phys.* **14**, 242–251 (2018).
20. W. F. Tsai, H. Lin, The integrity of two sides. *Nat. Mater.* **15**, 927–928 (2016).

21. S. Zhang, A. Baker, S. Komineas, T. Hesjedal, Topological computation based on direct magnetic logic communication. *Sci. Rep.* **5**, 15773 (2015).
22. O. G. Shpyrko, E. D. Isaacs, J. M. Logan, Y. Feng, G. Aeppli, R. Jaramillo, H. C. Kim, T. F. Rosenbaum, P. Zschack, M. Sprung, S. Narayanan, A. R. Sandy, Direct measurement of antiferromagnetic domain fluctuations. *Nature* **447**, 68–71 (2007).
23. S. Konings, C. Schüßler-Langeheine, H. Ott, E. Weschke, E. Schierle, H. Zabel, J. B. Goedkoop, Magnetic domain fluctuations in an antiferromagnetic film observed with coherent resonant soft x-ray scattering. *Phys. Rev. Lett.* **106**, 077402 (2011).
24. S.-W. Cheong, M. Fiebig, W. Wu, L. Chapon, V. Kiryukhin, Seeing is believing: Visualization of antiferromagnetic domains. *npj Quant. Mater.* **5**, 3 (2020).
25. S. Anders, H. A. Padmore, R. M. Duarte, T. Renner, T. Stammler, A. Scholl, Photoemission electron microscope for the study of magnetic materials. *Rev. Sci. Inst.* **70**, 3973–3981 (1999).
26. M. G. Kim, H. Miao, B. Gao, S.-W. Cheong, C. Mazzoli, A. Barbour, W. Hu, S. B. Wilkins, I. K. Robinson, M. P. M. Dean, V. Kiryukhin, Imaging antiferromagnetic antiphase domain boundaries using magnetic Bragg diffraction phase contrast. *Nat. Commun.* **9**, 5013 (2018).
27. M. Retuerto, S. Skiadopoulou, F. Borodavka, C. Kadlec, F. Kadlec, J. Prokleska, Z. Deng, J. A. Alonso, M. T. Fernandez-Diaz, F. O. Saouma, J. I. Jang, D. Legut, S. Kamba, M. Greenblatt, Structural and spectroscopic properties of the polar antiferromagnet $Ni_2MnTeO_6$. *Phys. Rev. B* **97**, 144418 (2018).
28. J. Kim, J. Yang, C. J. Won, K. Kim, B. Kim, D. Obeysekera, D. W. Lee, S.-W. Cheong, Helical versus collinear antiferromagnetic order tuned by magnetic anisotropy in polar and chiral $(Ni,Mn)_3TeO_6$. *Phys. Rev. Mater.* **5**, 094405 (2021).
29. T. Choi, Y. Horibe, H. T. Yi, Y. J. Choi, W. Wu, S.-W. Cheong, Insulating interlocked ferroelectric and structural antiphase domain walls in multiferroic $YMnO_3$. *Nat. Mater.* **9**, 253–258 (2010).
30. T. Jungk, A. Hoffmann, M. Fiebig, E. Soergel, Electrostatic topology of ferroelectric domains in $YMnO_3$. *Appl. Phys. Lett.* **97**, 012904 (2010).
31. O. G. Shpyrko, X-ray photon correlation spectroscopy. *J. Synchrotron Rad.* **21**, 1057–1064 (2014).
32. O. Bikondoa, On the use of two-time correlation functions for X-ray photon correlation spectroscopy data analysis. *J. Appl. Cryst.* **50**, 357–368 (2017).
33. P. Gaunt, Ferromagnetic domain wall pinning by a random array of inhomogeneities. *Philos. Mag. B* **48**, 261–276 (1983).
34. Y. Shen, G. Fabbris, H. Miao, Y. Cao, D. Meyers, D. G. Mazzone, T. A. Assefa, X. M. Chen, K. Kisslinger, D. Prabhakaran, A. T. Boothroyd, J. M. Tranquada, W. Hu, A. M. Barbour, S. B. Wilkins, C. Mazzoli, I. K. Robinson, M. P. M. Dean, Charge condensation and lattice coupling drives stripe formation in nickelates. *Phys. Rev. Lett.* **126**, 177601 (2021).
35. J. Li, J. Pelliciari, C. Mazzoli, S. Catalano, F. Simmons, J. T. Sadowski, A. Levitan, M. Gibert, E. Carlson, J.-M. Triscone, S. Wilkins, R. Comin, Scale-invariant magnetic textures in the strongly correlated oxide $NdNiO_3$. *Nat. Commun.* **10**, 4568 (2019).


**Acknowledgments:** We are grateful to J. Lin for assistance with x-ray experiments. **Funding:** This work was supported by the U.S. Department of Energy (DOE) grant nos. DE-FG02-07ER46382 (to M.G.K., V.K., and S.-W.C.) and DE-SC0021188 (to J.Y.). This research used resources at the 23-ID-1 (CSX) beamline of the National Synchrotron Light Source II, a DOE Office of Science User Facility operated for the DOE Office of Science by Brookhaven National Laboratory under contract no. DE-SC0012704. This work was also supported by the National Research Foundation of Korea (NRF) funded by the Ministry of Science and ICT grant nos. 2016K1A4A4A01922028 and 2020M3H4A2084417 (to C.J.W. and S.-W.C.); Engineering and Physical Sciences Research Council grant EP/I022562/1, "Phase modulation technology for X-ray imaging" 2011 to present; (to I.K.R.) and European Research Council Advanced grant number 227711, "Exploration of strains in synthetic nanocrystals" 2009 to present (to I.K.R.).
**Author contributions:** Conceptualization: V.K. and M.G.K. Methodology: V.K., M.G.K., and C.M. Investigation—sample synthesis: C.W., S.-W.C., and J.Y. Investigation—x-ray experiments: M.G.K., A.B., W.H., S.B.W., I.K.R., M.P.M.D., C.M., and V.K. Visualization: M.G.K. Supervision: V.K. Writing—original draft: V.K. Writing—review and editing: All authors. **Competing interests:** I.K.R. declares that he has competing interests as chair of the Science Advisory Committee of the ALBA Synchrotron, Barcelona, Spain and chair of the Science Advisory Committee of the European X-ray Free Electron Laser Facility in Hamburg at different times during the progress of this research and its extended publication process. I.K.R. also declares that he has competing interests as chairperson of the Royal Society Conference "Real and reciprocal space x-ray imaging"; organizer of the first UK-Japan Chromosome Imaging Workshop; chairperson of "Size-Strain VII" conference; chairperson of the Beamline Advisory Team, Bragg Coherent Diffractive Imaging at the National Synchrotron Light Source; and chairperson of the "Coherence 2018" conference, all overlapping the time of the research. I.K.R. also declares that he has competing interests as a member of the Editorial Board of IUCrJ (International Union of Crystallography Journal) and was the holder of the Gregori Aminoff Prize in Crystallography, Royal Swedish Academy of Sciences "for his development of diffraction techniques for the investigation of surfaces and nanomaterials" during the planning stage of the research. The authors declare that they have no other competing interests. **Data and materials availability:** All data needed to evaluate the conclusions in the paper are present in the paper and/or the Supplementary Materials. Numerical data are available on Zenodo, a publicly accessible repository, at https://doi.org/10.5281/zenodo.6425654.

Submitted 11 June 2021
Accepted 12 April 2022
Published 27 May 2022
10.1126/sciadv.abj9493